

Numerical and Experimental Investigations of Fluidic Thrust Vectoring Mechanism

Li Li^{a,b} and Tsutomu Saito^a

^aDepartment of Aerospace Engineering, Muroran Institute of Technology,
Muroran, Japan

^bDepartment of Mechanical Engineering, Dalian Jiaotong University,
Dalian, China

Abstract

The objective of this paper is to investigate the fluidic thrust vectoring (FTV) effects of a secondary jet on the primary flow in a converging-diverging nozzle. The experiments are performed with a nozzle pressure ratio (NPR) of 4–10, a secondary pressure ratio (SPR) of 1 or 2, and two different secondary jet locations. Numerical simulations of the nozzle flow are carried out by solving the Navier-Stokes equation, and the input parameters are set to match the experimental conditions. Computations are performed with and without the secondary jet injection for different combinations of NPR, SPR, and jet location. The thrust pitching moment is also determined to evaluate the FTV performance. It is found that the thrust pitching moment increases with the SPR. The numerical results clearly indicate two FTV mechanisms induce thrust pitching moments with opposite signs.

1. INTRODUCTION

The demand for aerospace power requires technological advancements in the design of high-performance aircraft. Thrust vectoring is emerging as a key technology for current and future aircraft. Thrust-vectoring (TV) nozzle control can be effective under all flight conditions yet can satisfy the design constraints of low cost, low noise, light weight, short take-off distances, and improved stealth characteristics [1–3].

Two known methods of thrust vectoring are mechanical thrust vectoring (MTV) and fluidic thrust vectoring (FTV). MTV is carried out by placing paddles, vanes, or spoilers in a jet exhaust or by deflecting the divergent flaps of the nozzle to divert the main flow. The mechanical parts used to deflect thrust not only add weight and complexity to the aircraft but also increase cost and maintenance requirements [4–6]. These factors have led researchers to investigate novel methods to achieve the same thrust vectoring capabilities without external moving parts. FTV is an alternative method that involves a directional alteration of the main flow by a secondary jet. The injected flow generates an oblique shock in the primary flow, which deflects the primary flow to some angle. Potentially, fluidic thrust-vectoring nozzles provide effective flow deflection yet eliminate the problems associated with mechanical parts [7–9].

In the present study, the FTV method involves the injection of a secondary flow downstream of the throat in the diverging section of the nozzle. The main flow is deflected as it passes through the oblique shock formed by the secondary injection [10–12].

The nozzle is a converging-diverging type with a rectangular cross section. The secondary fluidic injection for thrust vector control is realized on the upper diverging wall of the nozzle. The objectives of this study are to put forward an FTV mechanism based on the pressure difference between the upper and lower nozzle walls and to provide guidance for optimizing nozzle configuration. The interaction of the secondary injection with the primary flow in the nozzle is also discussed.

Complex wave interactions occur in the flow field downstream of the nozzle throat when the secondary jet is injected. Therefore, it is difficult to find a correlation between the secondary jet and measures of the

FTV performance such as the deflection angle of the exhaust gas flow. Consequently, in this study, the thrust pitching moment obtained by integrating the pressure over the upper and lower nozzle walls for an arbitrarily chosen pivot is used to evaluate the FTV performance. The pitching moment computed from the numerically obtained pressure distributions has a sign opposite to that expected from the aforementioned FTV mechanism that is induced by an oblique shock wave formed by the secondary jet. The pitching moment is generated by a large pressure imbalance in the region close to the nozzle exit. This is another FTV mechanism that must be considered in the design of FTV nozzles, and it is discussed in this paper.

2. EXPERIMENTAL PROCEDURE

2.1. Test equipment

A photograph of the experimental setup is shown in Fig. 1. The inlet of the nozzle is exposed to the atmosphere, whereas the outlet is connected to a vacuum tank. The vacuum tank has a large volume of 33 m^3 and the back pressure of the nozzle is kept practically constant at 0.1 atm during a typical test period of 5–10 s. Pressurized dry air is used as the gas source of the secondary jet. Figure 2 shows the structure of the FTV nozzle. The height of the nozzle throat is 10 mm, and the area ratio of the nozzle exit and the throat is 1.18. With this nozzle expansion ratio, the flow Mach number at the nozzle exit is expected to be 1.5 according to an inviscid quasi-one-dimensional analysis. The secondary jet injection slot on the upper nozzle wall has a width of 1 mm.

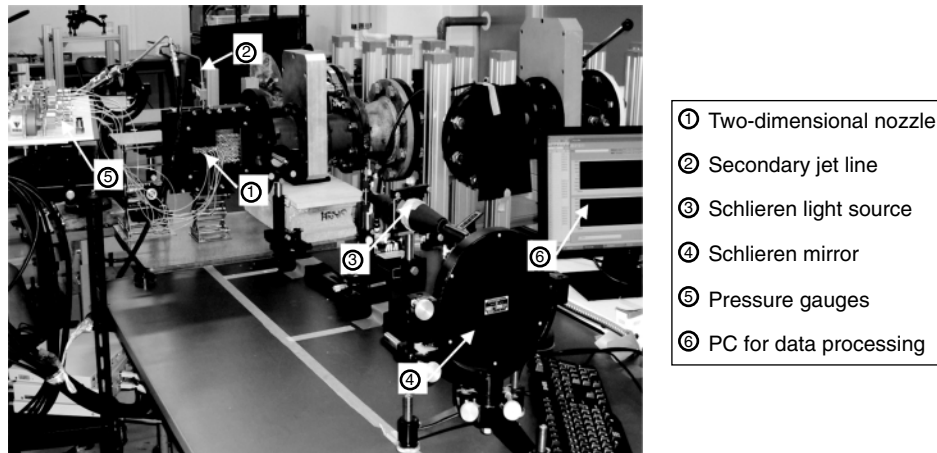


Figure 1. Experimental setup of FTV nozzle and measuring systems.

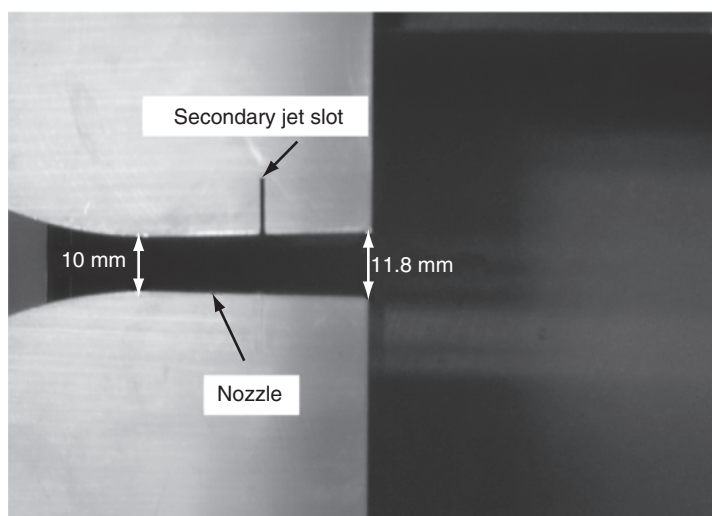


Figure 2. Photograph of two-dimensional nozzle.

2.2. Parameters in experiment and computation

The following conventions were used for data reduction. The nozzle pressure ratio (NPR) is the ratio of primary flow total pressure to nozzle back pressure, whereas the secondary pressure ratio (SPR) is the ratio of secondary jet total pressure to primary flow total pressure. The length L_j is the distance between the secondary jet injection slot and the nozzle exit. The conditions in the experiments and numerical simulations let the NPR range from 4 to 10 and the SPR was 1 or 2, with L_j set to 5 mm or 10 mm.

2.3. Instrumentation

The static pressure was measured using strain-type pressure gauges (PG-2KU and PG-20KU of Kyowa Electronic Instruments Co.). The rated capacities of the pressure gauges used in the main flow and secondary jet are 200 kPa and 2 MPa, respectively. The static pressure probes were spaced every 10 mm starting at 30 mm upstream of the nozzle throat and extending to downstream of the nozzle exit along the centerline of the nozzle. The pressure gauges were calibrated with a GE Sensing DPI610 Calibrator. All pressure data from the test nozzle were recorded simultaneously.

2.4. Flow visualization

A standard Schlieren system [13–14] was used to visualize the flow inside and downstream of the nozzle. A light ray from a point light source passed the first plane mirror, two concave mirrors on each side of the nozzle, the second plane mirror, and a knife edge, reaching either a digital camera (Nikon D40X) or a high-speed video camera (Photron Fastcam MAXP01).

3. NUMERICAL STUDY

3.1. Computational methods

The governing equations of the conservation laws for two-dimensional inviscid flows are expressed as

$$U_t + F_x + G_y = 0, \quad (1)$$

$$U = \begin{bmatrix} \rho \\ \rho u \\ \rho v \\ E \end{bmatrix}, \quad (2)$$

$$F = \begin{bmatrix} \rho u \\ \rho u^2 + p \\ \rho uv \\ u(E + p) \end{bmatrix}, \quad G = \begin{bmatrix} \rho v \\ \rho uv \\ \rho v^2 + p \\ v(E + p) \end{bmatrix}, \quad (3)$$

where ρ and p are the density and pressure, u and v are the x and y components of velocity, respectively, and E is the total energy per unit volume. The column vector U represents conserved quantities, while F and G are the fluxes in the x and y directions, respectively. When viscosity and heat conduction are added to the basic equations, F and G are modified to a Navier-Stokes conservation form such as

$$F = F^a - F^d, \quad G = G^a - G^d, \quad (4)$$

where the flux vectors F^a and G^a are the inviscid fluxes for the Euler equations as given by Eqn. (3). The flux vectors F^d and G^d associated with the viscosity and heat conduction are expressed as

$$F^d = \begin{bmatrix} 0 \\ \tau_{xx} \\ \tau_{xy} \\ u\tau_{xx} + v\tau_{xy} + kT_x \end{bmatrix}, \quad G^d = \begin{bmatrix} 0 \\ \tau_{yx} \\ \tau_{yy} \\ u\tau_{yx} + v\tau_{yy} + kT_y \end{bmatrix}, \quad (5)$$

where

$$\tau_{xx} = \frac{2}{3}\mu(2u_x - v_y), \quad \tau_{yy} = \frac{2}{3}\mu(2v_y - u_x), \quad \tau_{xy} = \tau_{yx} = \mu(u_y + v_x). \quad (6)$$

The components of the stress tensor τ are expressed as functions of the velocity gradients u_x, u_y, v_x, v_y and the coefficient of viscosity μ . Further, k is the thermal conductivity, while T_x and T_y are the x and y derivatives of temperature, respectively.

The Navier-Stokes equation is solved with the weighted average flux (WAF) method [15–16]. The numerical fluxes are evaluated with the HLLC approximate Riemann solver. The WAF scheme is one of the higher order extensions of the Godunov scheme, with second-order accuracy in both space and time.

3.2. Initial and boundary conditions

Initial and boundary conditions are defined to properly initialize and constrain the flow. The inflow boundary condition is set to atmospheric conditions. The pressure and other flow parameters at the nozzle exit are calculated from the NPR. The conditions are distributed over the flow domain as initial conditions. Figure 3 shows the boundary conditions of the entire flow field. In short, the inflow boundary condition means that the inlet is fixed to the atmospheric conditions, while the outflow boundary condition means that the flow is not reflected there. Further, the jet boundary condition is determined by the SPR, and the wall boundary condition means a reflective solid wall. Computations were carried out for combinations of NPR and SPR corresponding to those in experiments.

3.3. Numerical grids

Figure 4 shows the numerical grids around the secondary jet injection slot and the nozzle exit. In what follows, the nozzles with $L_j = 5$ mm and $L_j = 10$ mm are called Configuration 1 and Configuration 2, respectively. The grid cells allocated for the entire computational domain were 143,606 for

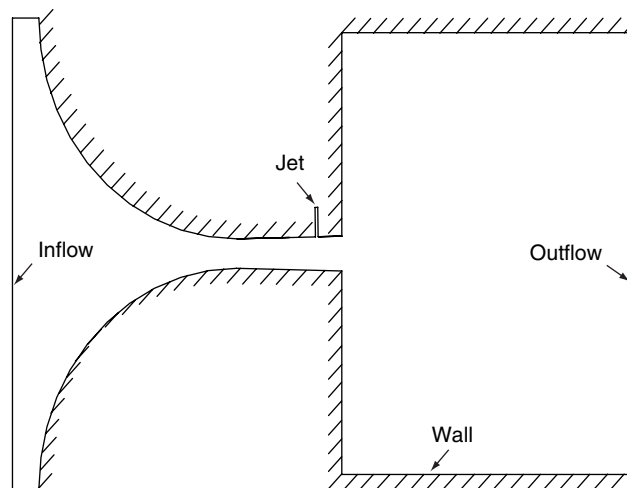


Figure 3. Boundary conditions.

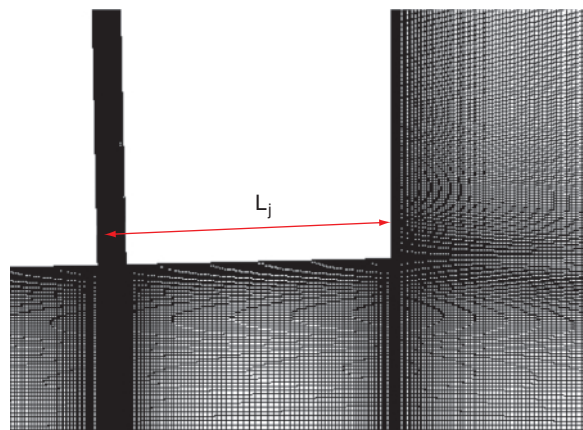


Figure 4. Grids around secondary jet (Config. 1 has $L_j = 5$ mm, Config. 2 has $L_j = 10$ mm).

Configuration 1 and 145,622 for Configuration 2. The calculation time was approximately 7 h to complete one case using 10 processing elements of a Cray XD1. The region downstream of the nozzle exit extends 0.11 m along the x -axis, and the height of the region is approximately 0.15 m.

4. RESULTS AND DISCUSSION

Experimental data were chosen for the two configurations, with NPR varied from 4 to 10 and SPR set to 1 or 2. Presented and discussed below are the static pressure on the nozzle wall, the thrust pitching moment, and the internal flow features (i.e., static pressure along the nozzle centerline, pressure distribution, Mach number distribution, and flow streamlines).

4.1. Nozzle performance without secondary jet

Figure 5 shows the static pressure along the nozzle centerline with NPR = 8. The pressure in the nozzle decreases from atmospheric pressure to back pressure. Since the back pressure is lower than the designed nozzle pressure (i.e., 0.027 MPa), the flow is under-expanded. It can be observed that the numerical and the experimental results are in good agreement with each other. The accuracy of the pressure gauges is approximately 1%, so the error bars are negligible in size as compared to the symbols in Fig. 5. The pressure distributions with other values of NPR have the same tendency.

4.2. Nozzle performance with secondary jet injection

4.2.1. Flows inside the nozzle

Figure 6 shows the schematics of the interaction between the secondary jet and the main flow in the diverging section of the nozzle with SPR = 1 and SPR = 2. In the nozzle upstream of the secondary injection, the boundary layer of the main flow is separated due to the adverse pressure gradient and with the generation of the oblique shock. This shock, the displaced boundary layer, the separation bubbles, and the secondary jet flow consequently form an obstruction in the diverging nozzle section. As shown in Fig. 6(a), with a small SPR, the jet flow is turned back toward the nozzle wall by the main flow. As shown in Fig. 6(b), as the SPR increases, the jet flow becomes parallel with the nozzle wall and extends out.

Figure 7 shows the pressure distributions for Configuration 1 with NPR = 8 and SPR = 1 or SPR = 2. The pressure upstream of the secondary jet slot increases with the SPR. As shown in Fig. 7(a), with a small SPR, not many wave interactions are observed in the diverging nozzle section. As shown in Fig. 7(b), as SPR increases, the high-pressure zone extends to the nozzle throat and forms complex wave interactions including shock waves. A noticeably low pressure is observed in the region close to the upper wall, between the jet injection point and the nozzle exit, as shown in Fig. 7(b). In the case of Configuration 2, the flow patterns are similar to those of Configuration 1, except that the oblique shock wave produced by the secondary jet reflects at the lower wall since the injection point has been shifted upstream by 5 mm. This is shown later in Figs. 9 and 10.

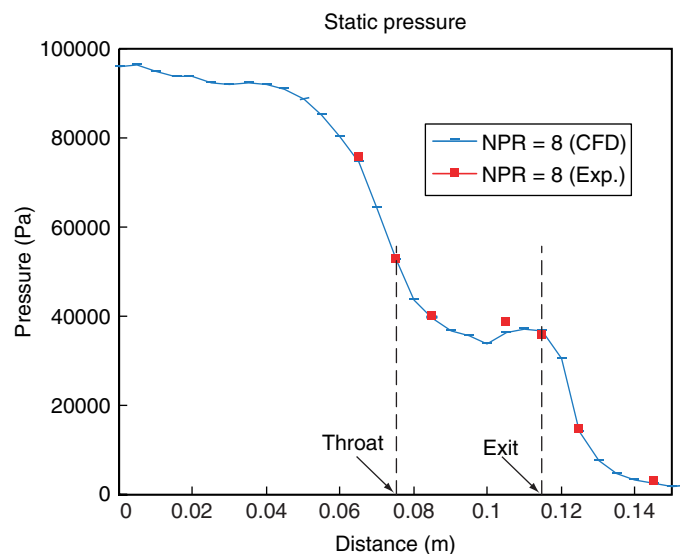


Figure 5. Static pressure at nozzle centerline without secondary jet.

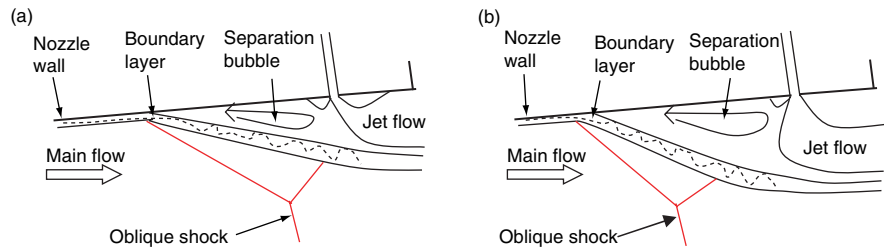


Figure 6. Interaction of secondary jet with primary flow at (a) $SPR = 1$ or (b) $SPR = 2$.

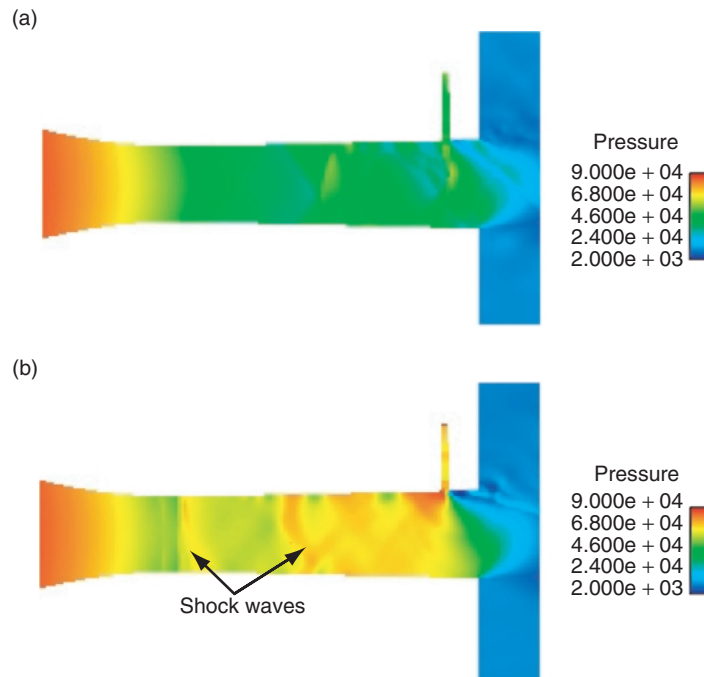


Figure 7. Static pressure distribution in diverging nozzle section with $NPR = 8$ and (a) $SPR = 1$ or (b) $SPR = 2$.

Figure 8 shows flow Mach number distributions for Configuration 1 with $NPR = 8$ and $SPR = 1$ or $SPR = 2$. The main flow accelerates in the converging section of the nozzle, reaching sonic speed at the nozzle throat and becoming supersonic downstream. As shown in Fig. 8(a), for a small SPR , even though there are some wave interactions in the diverging nozzle section, the effect of wave interactions on the flow velocity is small. Therefore, the flow remains supersonic throughout the diverging section. As shown in Fig. 8(b), as the SPR increases, a complex shock wave system is formed in the diverging section. The main flow is blocked by the secondary jet and becomes supersonic only for small regions in the diverging nozzle section and at the nozzle exit.

Figures 9 and 10 show the Schlieren images of Configurations 1 and 2, respectively, with $NPR = 8$. With $SPR = 1$, the secondary jet is visible as a dark line starting from the secondary jet slot in both Configuration 1 and Configuration 2, as seen in Figs. 9(a) and 10(a). The oblique shock wave is not clearly seen in Fig. 9(a) for Configuration 1, but it is clearly seen to reflect at the opposite nozzle wall in Fig. 10(a) for Configuration 2. With $SPR = 2$, the jet spreads extensively and the flow upstream of the injection slot is affected over a much wider region than with $SPR = 1$. The extent of the region is almost the same in Figs. 9(b) and 10(b); i.e., the region is simply shifted by the difference between the values of L_j in Configurations 1 and 2. Strong wave interactions, including shock waves, take place in the diverging nozzle section. However, despite the strong effect of the secondary jet, the deflection of the exhaust gas does not increase with the SPR in the present nozzle. A stronger effect does not necessarily mean a larger deflection.

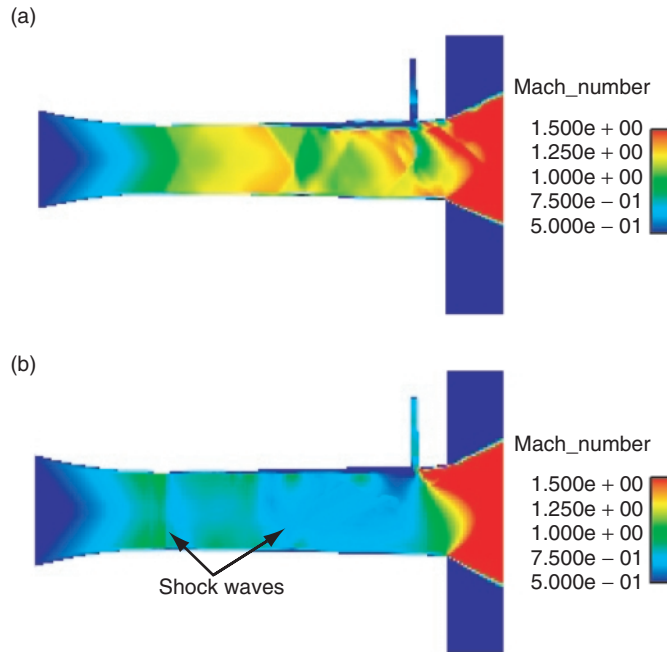


Figure 8. Mach number distribution in diverging nozzle section with NPR = 8 and (a) SPR = 1 or (b) SPR = 2.

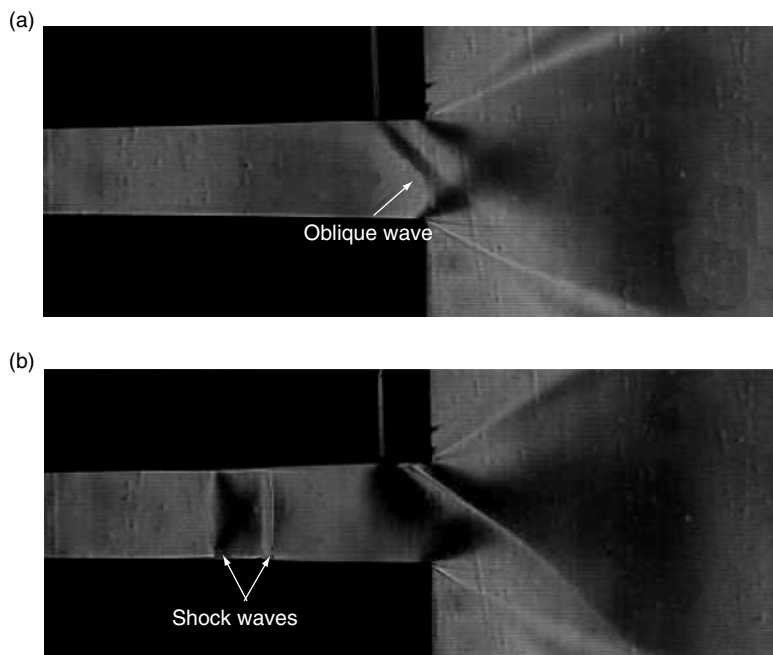


Figure 9. Schlieren images for Config. 1 with NPR = 8 and (a) SPR = 1 or (b) SPR = 2.

On the basis of this observation, we are now developing a new FTV nozzle. It has a relatively small injection slot so that the secondary jet does not block the main flow at the larger values of SPR. It is expected that more detailed investigations of the secondary jet effect will be carried out with this new nozzle.

In order to evaluate the effect of the oblique shock wave on the flow deflection, Fig. 11 compares the distributions of Mach number beyond the nozzle exit for Configurations 1 and 2 with SPR = 1. As expected, the Mach number at the nozzle exit is close to the designed value of 1.5. However, it is difficult to evaluate the thrust deflection angle directly from such flow patterns in the region

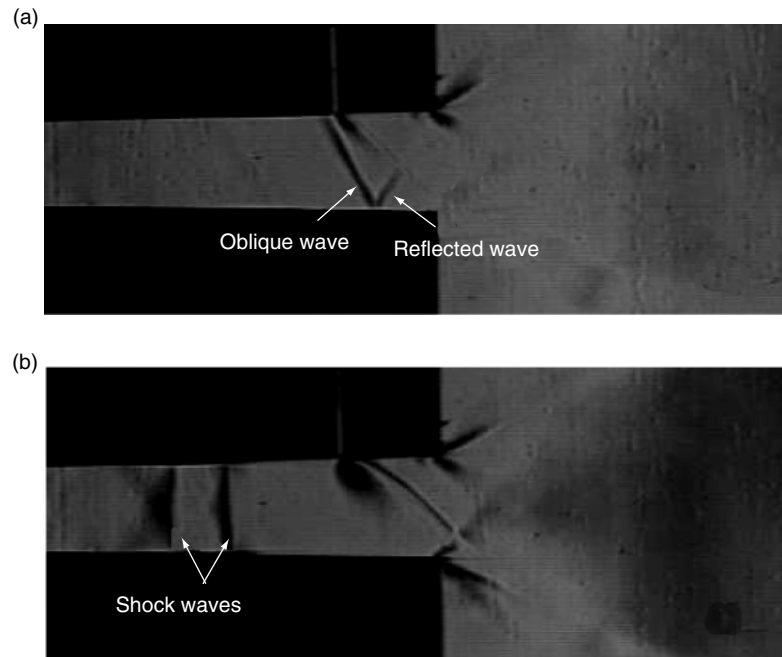


Figure 10. Schlieren images for Config. 2 with NPR = 8 and (a) SPR = 1 or (b) SPR = 2.

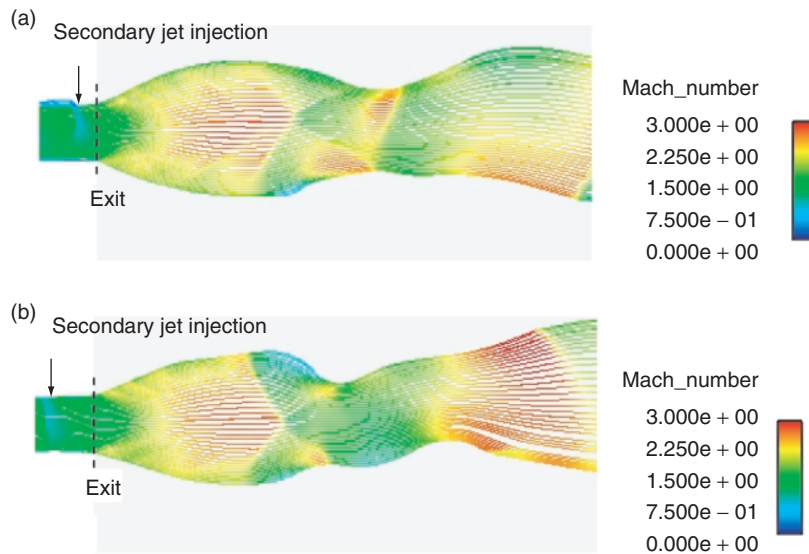


Figure 11. Mach number distribution and streamlines with NPR = 8 and SPR = 1 for (a) Config. 1 or (b) Config. 2.

downstream of the nozzle exit. In this study, therefore, we decided to evaluate the thrust angle by calculating the thrust pitching moment, as explained below.

4.2.2. Static pressure on upper and lower nozzle wall

Figures 12 and 13 show the numerical results for static pressure along the upper and lower nozzle walls in Configurations 1 and 2, respectively, with NPR = 8. For both SPR = 1 and SPR = 2, the pressure fluctuation shown in Fig. 12 is greater on the upper wall than on the lower wall. Additionally, the overall static pressure shown in Fig. 12(b) is higher than that shown in Fig. 12(a).

The static pressure on the upper wall is low between the secondary jet slot and the nozzle exit. This is most prominent in Fig. 12(b); i.e., for SPR = 2. The reason is that interaction between the secondary

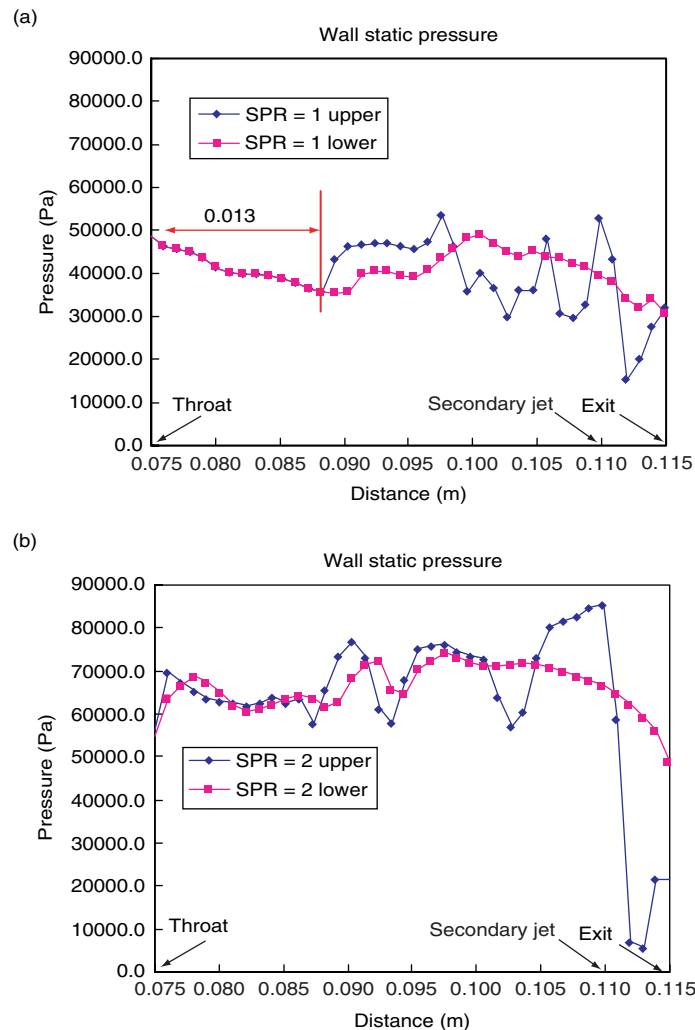


Figure 12. Wall pressure for Config. 1 with NPR = 8 and (a) SPR = 1 or (b) SPR = 2.

jet injection and the main flow creates an obstruction in the diverging section that makes it difficult for the main flow to pass the secondary jet flow. Hence, a low-pressure region is formed near the wall downstream of the jet slot, because of the suction by the much lower back pressure and the entrainment of air by the secondary jet, as shown in Fig. 6.

As seen in Figs. 12(a) and 13(a), both with SPR = 1, the pressure distribution curves overlap with each other for a region close to the throat where the pressure on the upper and lower walls is the same. These are the supersonic regions that are unaffected by the secondary jet injection. The region extends approximately 13 mm from the throat in Configuration 1, as shown in Fig. 12(a), and approximately 8 mm from the throat in Configuration 2, as shown in Fig. 13(a). This difference corresponds to the 5 mm upstream shift in the location of the secondary jet with the switch from Configuration 1 to Configuration 2.

As seen in Figs. 12(b) and 13(b), both with SPR = 2, the pressure distributions on the upper and lower nozzle walls are different throughout the entire region downstream of the nozzle throat. For the case SPR = 1, the pressure on the upper and lower walls at the nozzle throat is around 0.05 MPa, which corresponds to the theoretical choked value of 0.528 times the atmospheric pressure. However, for the case SPR = 2, the pressure on the nozzle wall at the throat is higher than the theoretical value, indicating that the flow is not choked. It can thus be concluded that the effect of the secondary jet injection pervades the entire diverging nozzle section only in the case of a large SPR. In the present experiments, the nozzle is not choked at the throat with SPR = 2.

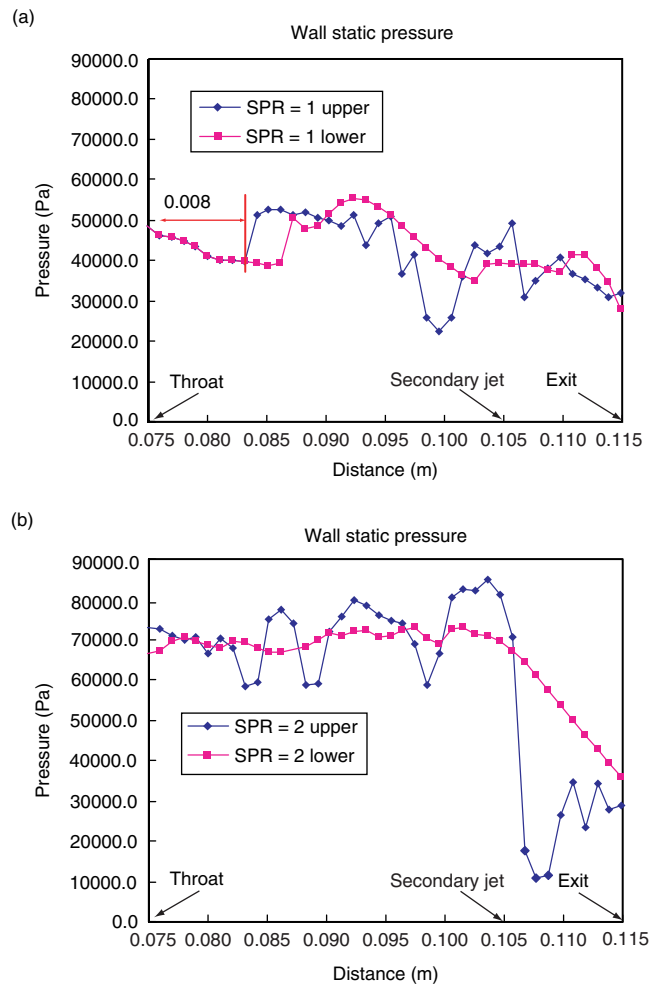


Figure 13. Wall pressure for Config. 2 with NPR = 8 and (a) SPR = 1 or (b) SPR = 2.

4.2.3. Thrust pitching moment

The thrust pitching moment of the nozzle is calculated by integrating the product of the pressure on the nozzle walls and the length from a specific pivot point to the pressure working point. The pivot point was chosen arbitrarily at 0.075 m upstream of the throat, and the moment was plotted for different values of NPR ranging from 4 to 10, as shown in Fig. 14. The following are thus observed: i) for a given configuration, the pitching moment increases with the SPR; ii) for SPR = 2, the pitching moment in Configuration 2 is greater than that in Configuration 1, except at NPR = 10; and iii) for SPR = 1, the moments in the two configurations are close, except at NPR = 5 and NPR = 9; however, they have a similar tendency of SPR = 2.

Note that the pitching moment is positive at most data points. It is negative at only three data points with large NPR values and with SPR = 1. In this study, a clockwise moment is defined as positive, so the strongly positive pitching moment is attributed to the low pressure on the upper wall between the secondary jet and the nozzle exit. In this area, the air flows outward due to the low back pressure outside the nozzle. At the same time, the gas in this area is entrained by the secondary jet and the pressure becomes noticeably low, as already shown in Fig. 13. Close to the exit, the pressure balance between the upper and lower walls makes the pitching moment positive.

With the current experimental setup, if the pitching moment is only induced by the deflection of the exhaust gas, then a negative pitching moment is expected, since the exhaust gas is deflected downward by an oblique shock wave. Based on these findings in the present experiments, thrust vectoring from the effect of pressure balance is much stronger than that from the deflection of exhaust gas by an oblique shock wave. A series of experiments with a new nozzle configuration is now in preparation for

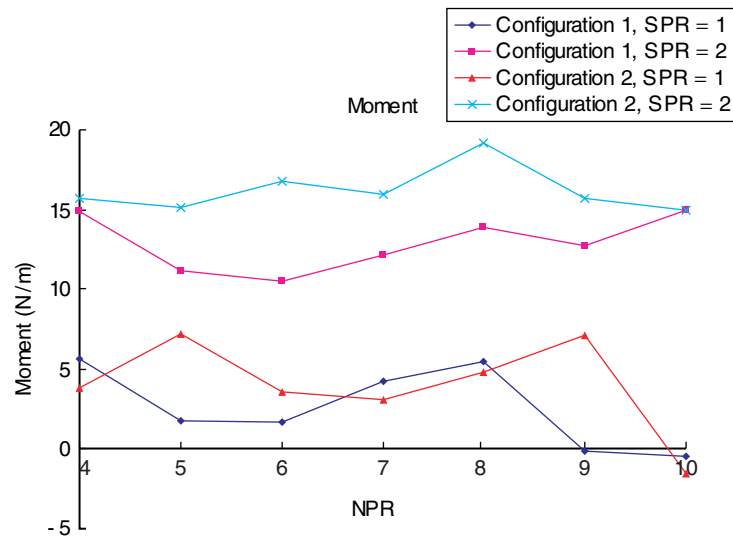


Figure 14. Thrust pitching moment.

an investigation of the relative performance of the FTV owing to each of the aforementioned mechanisms of pitching moment production.

5. CONCLUSIONS

Numerical and experimental studies of fluidic thrust vectoring were carried out with a simple two-dimensional nozzle model and a slot for injecting a secondary jet into the main flow.

It has been found difficult to quantitatively evaluate the FTV performance on the basis of the appearance of downstream flow patterns. In this study, the performance was instead evaluated from the thrust pitching moment.

In addition to the expected FTV mechanism owing to flow deflection by an oblique shock wave, a mechanism owing to the pressure difference in the vicinity of the nozzle exit was observed. The two mechanisms act in opposite directions, but the latter is much stronger in the current experimental setup.

The opening for the secondary jet injection is too large in the present setup, and the entire flow field downstream of the throat is affected by the jet even with a relatively low secondary jet pressure ratio; i.e., $SPR = 2$. In this study, the FTV mechanism attributed to flow deflection by an oblique shock is concealed by other complex wave interactions that are stronger. A new experimental model with a smaller secondary jet opening is now being constructed to study more clearly the details of the FTV mechanism and its performance.

ACKNOWLEDGMENTS

This research was partly supported by the Ministry of Education, Culture, Sports, Science and Technology through a Grant-in-Aid for scientific research(C) 21560162.

REFERENCES

- [1] Rickey J. Shyne, A Survey of Challenges in Aerodynamic Exhaust Nozzle Technology for Aerospace Propulsion Applications, NASA/TM-2002-211977.
- [2] K. A. Deere, Computational Investigation of the Aerodynamic Effects on Fluidic Thrust Vectoring, 36th AIAA/ASME/SAE/ASEE Joint Propulsion Conference and Exhibit, 2000.
- [3] David J. Wing, Victor J. Giuliano, Fluidic Thrust Vectoring of an Axisymmetric Exhaust Nozzle at Static Conditions, ASME Fluids Engineering Division Summer Meeting, 1997.
- [4] John S. Orme, Ross Hathaway, Initial Flight Test Evaluation of the F-15 ACTIVE Axisymmetric Vectoring Nozzle Performance, NASA/TM-1998-206558.
- [5] Scott C. Asbury, Francis J. Capone, Multiaxis Thrust-Vectoring Characteristics of a Model Representative of the F-18 High-Alpha Research Vehicle at Angles of Attack From 0° to 70° , NASA TP-3531, December 1995.

- [6] John S. Orme, Robert L. Sims, Selected Performance Measurements of the F-15 ACTIVE Axisymmetric Thrust-Vectoring Nozzle, Paper No. IS 166, 14th ISABE Annual Symposium, Florence, Italy, September 1999.
- [7] Karen A. Deere, Bobby L. Berrier, Computational Study of Fluidic Thrust Vectoring Using Separation Control in a Nozzle, 21st AIAA Applied Aerodynamics Conference AIAA-2003-3803, Orlando, FL, June 2003.
- [8] Jeffrey D. Flamm, Experimental Study of a Nozzle Using Fluidic Counterflow for Thrust Vectoring, AIAA 98-3255.
- [9] Mark S. Mason, William J. Crowther, Fluidic Thrust Vectoring of Low Observable Aircraft, CEAS Aerospace Aerodynamic Research Conference, 2002.
- [10] Kenrick A. Waithe, Karen A. Deere, Experimental and Computational Investigation of Multiple Injection Ports in a Convergent-Divergent Nozzle for Fluidic Thrust Vectoring, 21st AIAA Applied Aerodynamics Conference AIAA-2003-3802, Orlando, FL, June 2003.
- [11] P. J. Yagle, D. N. Miller, Demonstration of Fluidic Throat Skewing for Thrust Vectoring in Structurally Fixed Nozzles, ASME Journal of Engineering for Gas Turbines and Power, 2001, 123.
- [12] K. A. Deere, Computational Investigation of the Aerodynamic Effects on Fluidic Thrust Vectoring, 36th AIAA/ASME/SAE/ASEE Joint Propulsion Conference & Exhibit, Huntsville, AL, July 2000.
- [13] J. L. Caton, M. E. Franke, Flow Visualization of Transient Phenomena in Wind Tunnels, Instrumentation Society of American Symposium, Denver, CO, May 1990.
- [14] Schlieren photography, <http://www.anfoworld.com/Schliere>.
- [15] Eleuterio F. Toro, Riemann Solvers and Numerical Methods for Fluid Dynamics, 2nd edn., Springer-Verlag, Berlin, 1999.
- [16] E. F. Toro, A Weighted Average Flux Method for Hyperbolic Conservation Laws, Proceedings of the Royal Society of London A, 1989, 423, 401-418.